**ACCEPTED MANUSCRIPT**

# Gap width modification on fully screen-printed coplanar Zn|MnO2 batteries

# Gap width modification on fully screen-printed coplanar Zn|MnO2 batteries

*Patrick Rassek*[1,3], *Erich Steiner*[2], *Michael Herrenbauer*[1,2] *and Timothy C. Claypole*[3]

[1] Department of Packaging Technology, Stuttgart Media University, D-70569, Stuttgart, Germany
[2] Innovative Applications of the Printing Technologies, Stuttgart Media University, D-70569, Stuttgart, Germany
[3] Welsh Centre for Printing and Coating, College of Engineering, Swansea University, Swansea, SA2 8PP, United Kingdom

E-mail: rassek@hdm-stuttgart.de

## Abstract

Fully printed primary zinc-manganese dioxide ($Zn|MnO_2$) batteries in coplanar configuration were fabricated by sequential screen printing. While electrode dimensions and transferred active masses were kept at constant levels, electrode separating gaps were incrementally enlarged from 1 mm to 5 mm. Calendering of solely zinc anodes increased interparticle contact of active material within the electrodes while the porosity of manganese dioxide based electrodes was maintained by non-calendering. Chronopotentiometry revealed areal capacities for coplanar batteries up to 2.8 mAh cm$^{-2}$. Galvanostatic electrochemical impedance spectroscopy (GEIS) measurements and short circuit measurements were used to comprehensively characterise the effect of gap width extension on bulk electrolyte resistance and charge transfer resistance values. Linear relationships between nominal gap widths, short circuit currents and internal resistances were evidenced, but showed only minor impact on actual discharge capacities. The findings contradict previous assumptions to minimise gap widths of printed coplanar batteries to a sub-millimetre range in order to retain useful discharge capacities. The results presented in this study may facilitate process transfer of printed batteries to an industrial environment.

## 1 Introduction

Flexible, highly scalable printed electronics applications are considered key components in establishing a globally connected Internet of Things (IoT) [1–6]. Significant advances are reported in the fabrication of printed soft wearable sensing devices for the surveillance of vital physiological parameters in healthcare [7–16] and in professional sports [17]. The implementation of fully printed smart tags or Flexible Hybrid Electronics (FHE) devices for monitoring supply chains or temperature-controlled transports in food logistics [18–20] in major evolving markets may be entered soon [21]. Wireless operation and communication of active smart tags require integration of an independent power source at device level. Therefore, printed $Zn|MnO_2$ batteries are predestined to act as eco-friendly and product lifecycle customised power sources. Growing interest in printed smart tags is recognised due to the resource-saving additive nature of printing technologies. Though, market implementation of printed electronics devices is ultimately driven by the unit costs which need to compete with mass products based on silicon Integrated Circuits (IC).

High-volume print runs of printed electronics devices are preferred to be realised on continuously producing roll-to-roll machinery to ensure cost-effectiveness [22]. Fabrication of printed electronics devices on already installed conventional printing machines used in the field of graphic printing is the long-term objective [23]. However, products like screen-printed coplanar batteries set high demands on the registration accuracy of printing equipment. Due to physical connections, gap widths of less than 1 mm between anode and cathode are usually aspired to retain acceptable electrochemical battery performance characteristics [24, 25]. High-precision laboratory-scale printing equipment with optical positioning systems is required to ensure gap widths on this scale. Any incorrect positioning of

electrically conductive layers or displacement of electrode active material due to shifts in the registration would consequently result in battery malfunction.

The versatility of recently reported construction principles, electrode shapes and novel approaches to achieve rechargeability of this battery chemistry [25–27] reflects the substantial interest in printed Zn|MnO₂ batteries. Saidi et al. [28] report on screen-printed primary Zn|MnO₂ batteries in coplanar configuration. Comprehensive studies on electrode design characteristics and printed MnO₂:Zn mass ratios are presented with respect to battery discharge capacities. Printed single cells were activated by applying liquid (5.6 M) or gel-like (8.0 M) alkaline potassium hydroxide (KOH) electrolytes. Increased battery discharge capacities were recorded when both electrodes covered equal areas on printed current collectors instead of the Zn anodes being separated in fractional areas. Examined batteries were discharged to an extended cut-off voltage (COV) of 0.75 V and delivered maximum discharge capacities up to 19 mAh [28].

Lao-atiman et al. [29] present an innovative approach of screen-printed stack-type Zn|MnO₂ batteries with transparent current collectors, electrodes and electrolyte. The authors ensured transparency of the batteries by printing of micro-electrode arrays with a size of (50 x 50) µm which is below the resolution limit of the human eye. Screen-printed electrodes were varied in a thickness range of 30-80 µm while current-voltage characteristics of the batteries were studied in response to the transparency. Open circuit potentials (OCPs) up to 1.25 V could be achieved and a battery with 80 % opening area delivered a maximum energy density of 3.16 mWh cm⁻² at 1 mA cm⁻². Working batteries could be demonstrated, but Lao-atiman et al. admitted that the presented "[…] method may not be feasible for mass production on account of cost inefficiency and high level of complexity [29]."
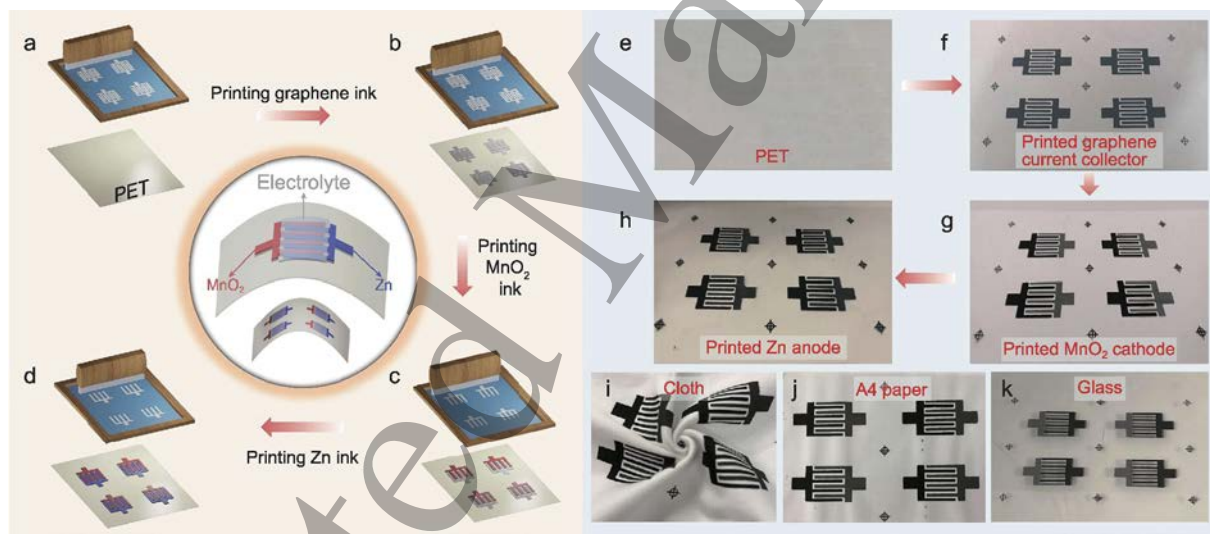


*Figure 1 Fabrication of printed Zn|MnO₂ coplanar micro-batteries (MBs). (a–d) Schematic of screen-printing fabrication of printed Zn|MnO₂ MBs: (a) the blank PET substrate; (b) the printed graphene current collectors; (c) the printed MnO₂ cathode and (d) the printed Zn anode. (e–h) Optical photographs showing the stepwise printing fabrication of Zn|MnO₂ MBs: (e) the blank PET substrate; (f) the graphene current collectors; (g) the printed MnO₂ cathode and (h) the printed Zn anode on interdigital graphene fingers. (i–k) Zn|MnO₂ MBs printed onto different substrates, including (i) cloth; (j) A4 paper, and (k) glass. Figure reproduced from Wang et al. [25] and licensed under CC BY 4.0.*

Wang et al. [25] present highly flexible secondary coplanar Zn|MnO₂ micro-batteries (MBs) with metal-free graphene-based current collectors printed on a variety of substrates including PET, glass, cloth and paper (Figure 1i-k). An interdigital battery layout comprising of eight fingers and a gap width of 1 mm between the electrodes was selected and created by screen printing (Figure 1a-g). Battery activation was realised by application of a mixture of 2 M zinc sulphate (ZnSO₄) and 0.5 M manganese sulphate (MnSO₄) as the aqueous electrolyte. Rechargeability of the Zn|MnO₂ battery chemistry was obtained by an intercalation process with insertion/extraction of Zn²⁺ ions in the porous structure of MnO₂ based cathodes. MBs were printed in single-cell configuration and in multi-cell series and parallel

2

configurations. Fabricated single-cell batteries demonstrated discharge plateaus of 1.3 V even under bending stress. A capacity retention of 83.9 % is reported after performing 1,300 cycles at 5C for a single-cell battery. Due to safety and low-cost of the raw materials Zn and $MnO_2$, Wang et al. see in printed $Zn|MnO_2$ batteries "[…] great potential as next-generation microscale power sources in various wearable, flexible, miniaturized and printed electronics [25]."

Various others performance affecting parameters of screen-printed $Zn|MnO_2$ batteries have been investigated in recent years [5, 27, 30–32]. Research efforts include the optimisation of printing ink formulations [31, 33], electrode shapes [24, 34], printing substrate characteristics [30, 35] and the evaluation of nonwoven and hydrogel separators [32]. The effect of gap width extension on battery performance metrics of printed coplanar $Zn|MnO_2$ batteries has not yet been subject of research.

In the present study, the nominal gap width of fully screen-printed zinc chloride ($ZnCl_2$) operated coplanar $Zn|MnO_2$ batteries is increased in increments of 1 mm in the range of 1 mm to 5 mm. Gap length and geometrical electrode areas are kept constant for all batteries (Figure 2c). Galvanostatic electrochemical impedance spectroscopy measurements and chronopotentiometry are systematically used to investigate the mechanism of the gap width variation on corresponding battery performance parameters discharge capacity $Q_{out}$, internal resistance $R_{in}$, and short circuit current $I_{sc}$. In accordance with the results of our previous experiments [36], all batteries of this experimental series comprise of a calendered Zn electrode and non-calendered $MnO_2$ cathodes. Typically, primary $Zn|MnO_2$ batteries are discharged to the COV of 0.9 V. Here, we discharged the batteries by chronopotentiometry to a COV of 0.6 V to determine potentially useful discharge capacity beyond the 0.9 V battery potential. The current load ability of prepared batteries with varying gap widths is investigated by applying constant discharge currents (CC) of 0.2 mA and 0.4 mA. The presented coplanar battery layout with an overall thickness of 0.5 mm is free of manual pick-and-place technologies which simplifies transfer of the lab-scale printing process to an industrial-scale production. Moderate requirements on registration accuracy conditioned by battery gap width extension can additionally improve machinability on already installed industrial-scale screen printing equipment. The innovation of this work may contribute to enhance cost-effectiveness and thus possible market implementation of this battery technology to power disposable wearable PE or FHE applications.

## 2 Materials and methods

### 2.1 Battery design

The main advantage of coplanar batteries is the redundancy of the application of a printed or mechanically placed separator on and between the electrodes. Figure 2a and b provide information on the construction principle selected for the printed coplanar batteries. Current collectors are realised by printed silver layers beneath subsequently printed carbon black passivation layers circumferentially overlapping the silver patterns by 0.3 mm. For all fabricated batteries examined in this experimental series, the geometrical area of the $MnO_2$ cathode is set to 32 $cm^2$ and 12 $cm^2$ for the Zn anode. The gap length was set to 80 mm. Electrochemical activation of the batteries is realised by printing of a gel-like 5.8 M $ZnCl_2$ electrolyte ink on top of the electrodes and in the separating gap as illustrated in Figure 2a. Encapsulation of the batteries is realised by direct lamination with a 75 μm thick two-layered composite substrate comprising of 37.5 μm PET and 37.5 μm ethylene-vinyl acetate (EVA).

The pursued gap width extension from 1 mm to 5 mm in increments of 1 mm is achieved by an opposing shift of the current collectors and passivation layers as illustrated by the magenta-coloured arrows in Figure 2c. Therefore, screen printing forms were prepared for current collectors and passivation layers for each individual gap width variation. Printing inks and relevant printing process parameters were kept constant for all printed battery variations. This procedure enables determination of differences in battery performance metrics in relation to the varying gap widths.
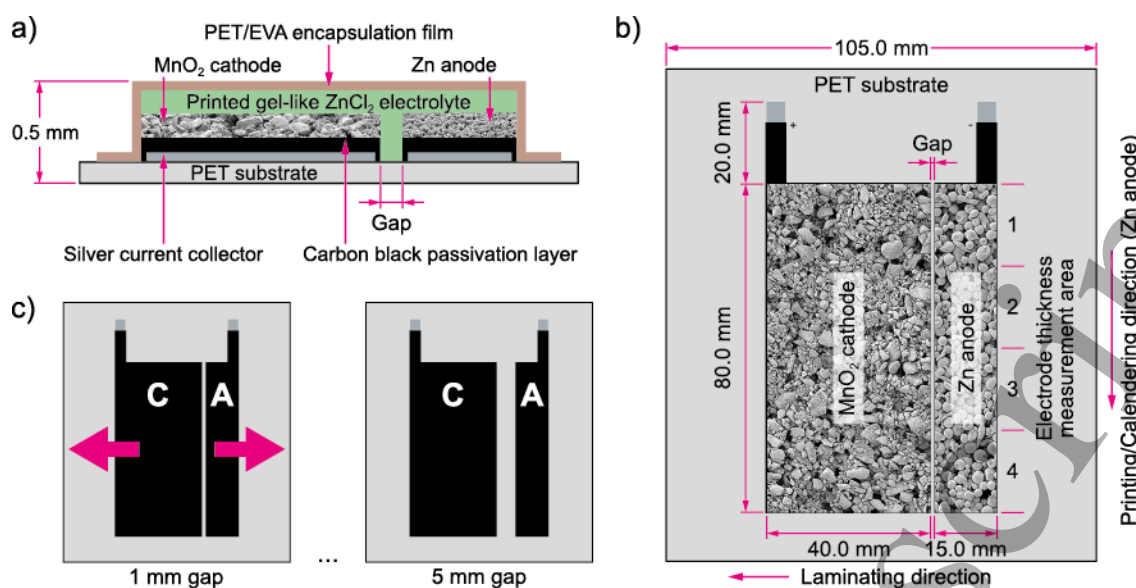
*Figure 2 (a) Cross-sectional view of the coplanar construction principle of the printed Zn|MnO₂ batteries; (b) top view of battery and electrode dimensions indicating directions of printing, calendering (Zn anode) and lamination; (c) illustration of the procedure used for gap width extension. Geometrical areas of the current collectors for the cathode C and anode A are kept constant as well as the gap length between both electrodes. (a, b) adopted from Rassek et al. [36].*

## 2.2 Galvanic inks

Battery grade G 007-pe Zn dust provided by Grillo Werke AG (Goslar, Germany) was used as electrode active material for the preparation of the water-based galvanic Zn ink. The G 007-pe Zn dust consists of spherical Zn particles with an average $d_{50}$ particle size of 27.5 µm [37]. Initially, double distilled water (ddH₂O) was emulsified by the addition of binding and thickening agents in a Dispermat LC30 dissolver equipped with a Polypropylene (PP) coated dissolver disc (VMA Getzmann, Reichshof, Germany). Sunrose MAC500LC sodium carboxymethylcellulose (Nippon paper Industries Co., Ltd, Tokyo, Japan), TRD1002 styrene butadiene rubber (SBR; JSR Corporation, Tokyo, Japan) and ddH₂O in a weight ratio of 2.8/5.8/91.4 were mixed until the emulsion reached a homogeneous consistency. Under stirring, G 007-pe Zn dust was slowly added until a weight ratio of 20/80 between emulsion and Zn was achieved.

For the preparation of the galvanic cathode ink, battery grade electrolytic manganese dioxide (EMD) powder blended with graphite UF4 was provided as electrode active component by Varta Microbattery GmbH (Ellwangen, Germany). The porosity of the MnO₂ and UF4 graphite particles of the cathode powder mixture requires an increase of the weight share of binders and solvent in contrast to the Zn ink. The MnO₂/UF4 powder mixture was continuously added under stirring to an afore prepared emulsion of MAC500LC Na-CMC, TRD1002 SBR and ddH₂O (2.8/5.8/91.4 wt.%) until a 70/30 weight ratio was reached.

## 2.3 Printing experiments and electrode processing

Flexible PET sheets of Melinex 339 (Dupont Teijin Film, Chester, USA) with a thickness of 175 µm were selected as printing substrate for the batteries. Printing experiments were performed on an EKRA E2 semi-automatic screen and stencil printing machine (Ekra Automatisierungssysteme GmbH, Bönnigheim, Germany) equipped with a manual optical positioning system.

Gap width variation of the coplanar battery layout (Figure 2c) was realised by repeated preparation of the same printing forms for the current collectors and passivation layers with the individual layouts. Silver current collectors were realised by printing of thin silver layers with a Henkel Loctite Electrodag E&C PF 050 conductive silver ink (Henkel AG & Co. KGaA, Düsseldorf, Germany). After drying of the silver layers (15 min, 120 °C), protective carbon black passivation layers were printed with a single print stroke on top of the silver current collectors with a Henkel Loctite Electrodag E&C PF 407 C carbon black ink. Water-based galvanic Zn and MnO₂ inks were each printed with the same printing

4

forms for all battery configurations. A more detailed description of the printing form fabrication process is provided in section 1.1 in the supplementary information.

Electrode fabrication started with printing of the galvanic Zn ink with a single print stroke. After drying of the Zn electrode layers (10 min, 80 °C), electrode compaction was realised by calendering of printed Zn layers with a 2-roll semi-automatic lab-scale supercalender in a nip set to 0.2 mm. Battery samples with the printed Zn anodes were fed through the calender with a roller speed of $35 \, \mathrm{mm \, s^{-1}}$. The calendering process and the effect of calendering on printed electrode layer characteristics is described in detail in [36]. $MnO_2$ cathodes were subsequently printed with double prints wet-on-dry to increase the $MnO_2$:Zn mass ratio of active material.

## 2.4 Battery activation and assembly

Initially, a 5.8 M $ZnCl_2$ aqueous electrolyte solution was prepared by dissolving weighted $ZnCl_2$ in crystalline form (Carl Roth GmbH, Karlsruhe, Germany) under stirring in $ddH_2O$ until a clear solution was formed. After cooling, the electrolyte solution was gelled by the addition of 4.4 wt.% of amorphous pyrogenic silica ($SiO_2$; Marabu GmbH & Co. KG, Tamm, Germany) to increase viscosity. The electrochemical activation of the $Zn|MnO_2$ batteries was realised by screen printing of electrolyte layers with a single print stroke on the electrode surfaces and the gap (Figure 3a). After drying of the electrolyte layers in a drying cabinet (75 s, 50 °C), batteries were directly encapsulated by lamination with a heated (110 °C) GBC Catena 35 roll laminator (ACCO Brands Corporation, Lake Zurich, USA). Determined water vapour transmission rates (WVTR) in the range of $4.7 \, \mathrm{g \, m^{-2}}$ per day demonstrated sufficient barrier properties of the 75 μm thick two-layered composite substrate (37.5 μm PET, 37.5 μm EVA) used to encapsulate the batteries from the front side. Moisture loss from the rear side of the battery may also be excluded by a low WVTR of $0.9 \, \mathrm{g \, m^{-2}}$ per day determined for the PET substrate with printed layers of current collectors and carbon black passivation layers. Additional information on WVTR measurements is provided in section 1.2 in the supplementary information.



*Figure 3 Activation and characterisation process of the screen-printed Zn/MnO₂ batteries: (a) placement of the electrolyte ink on the screen printing form prior to printing; (b) quick performance check to determine OCP and R<sub>in</sub> values; (c) batteries connected to the Bio-Logic BCS-805 battery tester for electrical and electrochemical characterisation.*

## 2.5 Electrical and electrochemical characterisation

Quick performance measurements were conducted on batteries with a Hioki BT3562 battery hitester (Hioki E.E. Corporation, Ueda, Japan) before and after encapsulation to exclude possible damage to electrodes during the encapsulation procedure. By using the four-terminal sensing 1 kHz alternating current (AC) method [38], internal resistance $R_{in}$ values and the OCP of fabricated batteries were validated as exemplarily shown in Figure 3b.

Chronopotentiometry (CP) experiments were performed on a Bio-Logic BCS-805 battery tester (Bio-Logic Science Instruments, Seyssinet-Pariset, France) by applying constant discharge currents of 0.2 mA and 0.4 mA (Figure 3c). In this study, the COV was extended to 0.6 V to identify useful capacity beyond the typically set COV of 0.9 V [39]. As illustrated in Figure 4, comprehensive galvanostatic electrochemical impedance spectroscopy (GEIS) measurements in a frequency range of 100 kHz – 10 mHz were conducted on a Bio-Logic SP-300 potentiostat at five different states of charge (SOC).

5
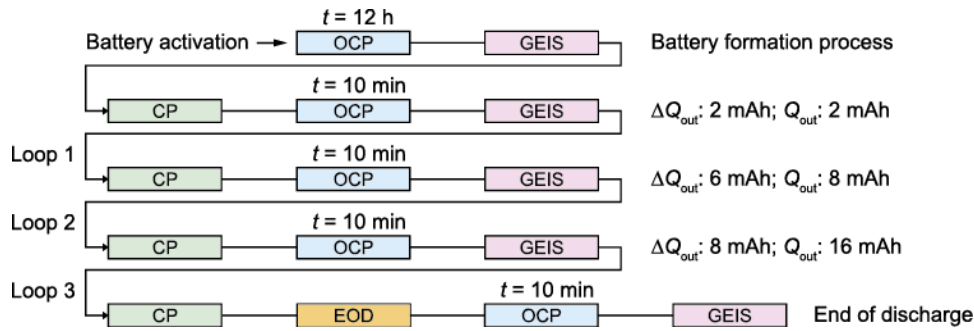
*Figure 4 Sequences of electrical and electrochemical battery characterisation with connected phases of chronopotentiometry (CP), open circuit potential (OCP) and galvanostatic electrochemical impedance spectroscopy (GEIS) in three loops to the end of discharge (EOD).*

The effect of gap width extension on battery pulse load ability was investigated by direct current (DC) short circuit current $I_{sc}$ measurements using a BK Precision 2709B digital multimeter (B&K Precision Corporation, Yorba Linda, USA). DC $I_{sc}$ measurements were conducted 12 h after battery encapsulation by lamination was performed. Such analysed batteries were discarded from further characterisation by GEIS or discharge measurements.

### 2.6 Microscopic studies

Layer thicknesses of calendered Zn electrode layers and non-calendered $MnO_2$ cathode layers were determined with a Keyence VK-9700K colour 3D laser microscope (Keyence Corporation, Osaka, Japan). Large-area imaging of electrodes before and after discharge was performed with a Cellcheck CIL-USB microscope (M-Service & Geräte, Meckenheim, Germany). Scanning electrode microscopy (SEM) studies of discharged batteries were conducted with a Tescan VEGA3 SEM using the scanning electron (SE) detector (Tescan GmbH, Dortmund, Germany).

## 3 Results and discussion

### 3.1 Physical characterisation of electrodes

Transferred dry masses of printed electrode layers were determined with an Ohaus AP2105 analytical balance (Ohaus GmbH, Greifensee, Switzerland). Overall, 125 battery samples were analysed in this experimental series. Examination of electrode layer thickness by laser scanning microscopy (LSM) was subdivided into four measurement areas arranged in electrode length as illustrated in Figure 2b. The whiskers of the corresponding box plots in Figure 5b indicate the ranges of determined electrode layer thicknesses from the beginning (maximum) to the end of printing image length (minimum).

Consistent processability of the Zn ink by screen printing is reflected by a constant mass transfer within the complete measurement series. As depicted in Figure 5a, average masses in the range of 0.47 g to 0.50 g with low standard deviations were determined for the Zn anodes. An average Zn electrode layer thickness of $(80.2 \pm 2.0)$ µm was achieved for all batteries after electrode compaction by calendering (Figure 5b). Within the individual battery series of different gap widths, measured Zn layer thickness values range from 77.4 µm (4 mm gap width) to 82.4 µm (3 mm and 5 mm). Mean Zn layer thickness ranges of around 15 µm were found in printing direction over the entire electrode length for all batteries except for the 4 mm series (Figure 5b).
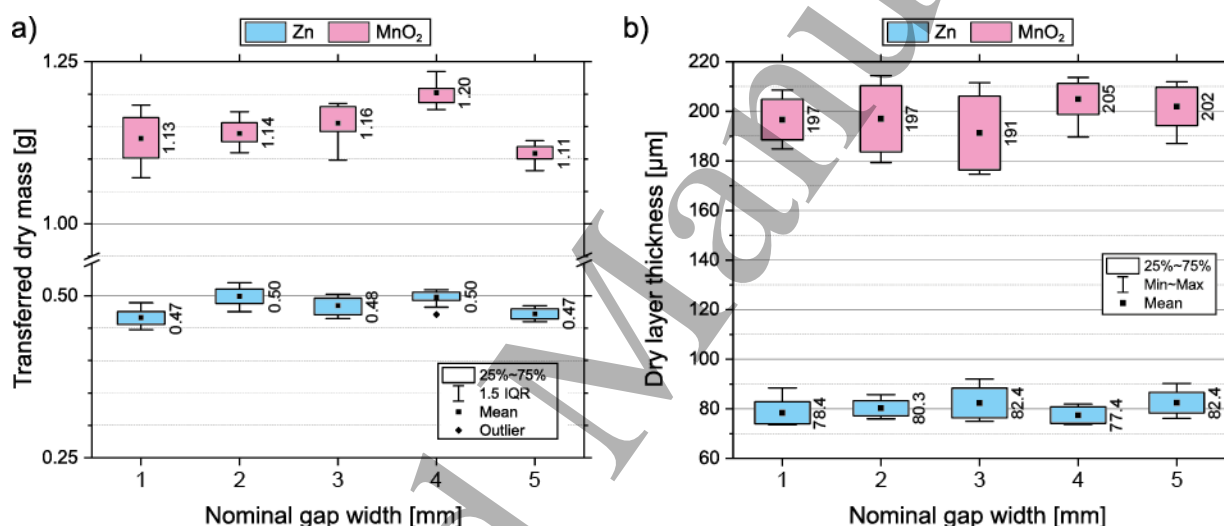


*Figure 5 (a) Transferred dry masses of electrode materials for the Zn and MnO$_2$ electrodes; (b) mean dry layer thickness values of the Zn anode and MnO$_2$ cathode layers. Whiskers indicate ranges between maximum and minimum layer thickness values determined at the beginning and the end of electrode printing image length. Extended ranges of non-calendered MnO$_2$ cathodes are attributed to distinctive mesh marking characteristics of electrode layers.*

Transferred masses of MnO$_2$ electrodes were increased to a considerable extent by the modification of the printing process to wet-on-dry double prints with intermediate drying (Figure 5a). While an average MnO$_2$ electrode mass of 0.64 g was achieved with a single print [36], this value was nearly doubled to 1.15 g when averaged for all battery configurations fabricated in this study. Mean values of individual battery versions range from 1.11 g (5 mm) to 1.20 g (4 mm). MnO$_2$ electrodes were not calendered to maintain the porous structure of the electrode material. As a result, dry layer thickness values substantially exceed the values of the Zn anodes (Figure 5b). Averaged for all batteries, 198 µm thick cathode layers ranging from 191 µm (3 mm) to 205 µm (4 mm) were transferred by double prints. Increased ranges of layer thickness of MnO$_2$ cathodes can be attributed to extended mesh marking characteristics of the dry electrode layers finding their peak with 37 µm at the 3 mm battery version.

Table 1 provides capacity related electrode parameters derived from battery electrode masses presented in Figure 5a. As can be seen, the target mass ratio MnO$_2$:Zn of 2.66 could not be achieved for fabricated batteries even with double prints wet-on-dry. Mean mass ratios range from $2.28 \pm 0.04$ (2 mm) to $2.43 \pm 0.07$ achieved for batteries having a nominal gap width of 1 mm. As a result of the slightly missed

target mass ratio, the amount of $MnO_2$ is the capacity limiting factor of the respective batteries [39]. Theoretical capacities $Q_{th}$ of electrodes were calculated in Table 1 by using the electrochemical equivalents (ECE) of Zn (3.24 g (Ah)$^{-1}$) and $MnO_2$ (1.22 g (Ah)$^{-1}$) and the average mass values of the respective electrodes shown in Figure 5a. Based on these figures, a $Q_{th}$ of $(353.8 \pm 9.7)$ mAh can be assumed for batteries of this experimental series. In reverse, an excess in printed Zn anode mass of $(0.05 \pm 0.01)$ g is available on the negative electrode side. Excessive Zn masses cannot be converted by electrochemical reaction (equation 1) due to mass related limitations of the $MnO_2$ cathodes. However, minor deviations of $Q_{th}$ of $MnO_2$ cathodes within the complete battery series can be classified as acceptable with respect to the expected discharge capacities.

$$4\,Zn + 8MnO_2 + 9H_2O + ZnCl_2 \rightarrow 8MnOOH + ZnCl_2 \cdot 4ZnO \cdot 5H_2O \qquad (1)$$

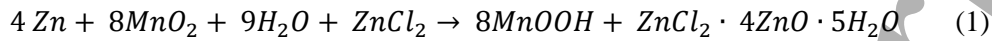*Table 1 Battery capacity determining electrode parameters. Theoretical capacities $Q_{th}$ of electrodes were calculated according the material specific electrochemical equivalents (ECE).*

| Nominal gap width [mm] | Mass ratio $MnO_2$:Zn | Averaged theoretical capacity $Q_{th}$ [mAh] | | $\Delta Q_{th}$ [mAh] | Excess Zn anode mass printed [g] |
| --- | --- | --- | --- | --- | --- |
| | | Zn anode | $MnO_2$ cathode | | |
| 1 | $2.43 \pm 0.07$ | 382 | 348 | 34 | 0.04 |
| 2 | $2.28 \pm 0.04$ | 409 | 351 | 58 | 0.07 |
| 3 | $2.38 \pm 0.07$ | 397 | 356 | 41 | 0.05 |
| 4 | $2.42 \pm 0.05$ | 407 | 370 | 37 | 0.05 |
| 5 | $2.35 \pm 0.03$ | 386 | 341 | 45 | 0.06 |

## 3.2 Electrical characterisation

### 3.2.1 Discharge characteristics

Figure 6a-d present discharge profiles of fabricated battery configurations achieved with 0.2 mA (Figure 6a, b) and 0.4 mA (Figure 6c, d) CC discharge experiments performed under identical ambient conditions. With respect to the discharge capacity drawn from the batteries, discharge curves of the most and the least efficient batteries of each measurement series were plotted in individual charts.

In Figure 6a, battery versions with gap widths of 3 mm and 4 mm show extended discharge capacities of 129.5 mAh respectively 134.0 mAh. In relation to the maximum available theoretical capacity $Q_{th}$, discharge efficiencies ($Q_{out}/Q_{th}$) of 36.4 % (3 mm) and 36.2 % (4 mm) were retrieved at the EOD. Moreover, both batteries show discharge capacities of more than 120 mAh before passing the 0.9 V potential limit which is typically set as the COV for Zn|$MnO_2$ batteries [39]. Discharge curves of batteries with gap widths of 2 mm and 5 mm are characterised by sloping profiles. As expected by theory, the battery comprising the largest gap width of 5 mm reveals the lowest discharge capacity with 99.3 mAh at 0.6 V EOD (29.1 % discharge efficiency). Information on parameters affecting discharge curve progression is provided in section 1.3 in the supplementary information. Compared to the other batteries examined, the closed circuit voltage (CCV) shows an accelerated drop in magnitude especially beyond the 1.1 V battery potential (Figure 6a). This is attributable to an increase in electrical resistance and a decrease in mass transport characteristics caused in this case by the enlarged distance between both electrodes [39]. Regardless of the gap width of the respective battery, all discharge curves show a more or less extensive kink located in the potential range of 0.8 V-0.7 V. Similar curve characteristics for stack type Zn|$MnO_2$ batteries were observed by [35, 40] and can be attributed to a two-phase $MnO_2$ reduction reaction [40].

Figure 6b shows discharge profiles of the least efficient batteries discharged with a 0.2 mA CC. Unexpectedly, all batteries show bare differences in curve progressions until 30 mAh are extracted by

8

discharge. Except for the battery version having a gap width of 4 mm, discharge curves are characterised by only slightly depressed voltage levels compared to the profiles presented in Figure 6a. Marginal decline in $Q_{out}$ of 5 mAh to 129.0 mAh is observed for the 4 mm battery version thus confirming a very consistent discharge capability.
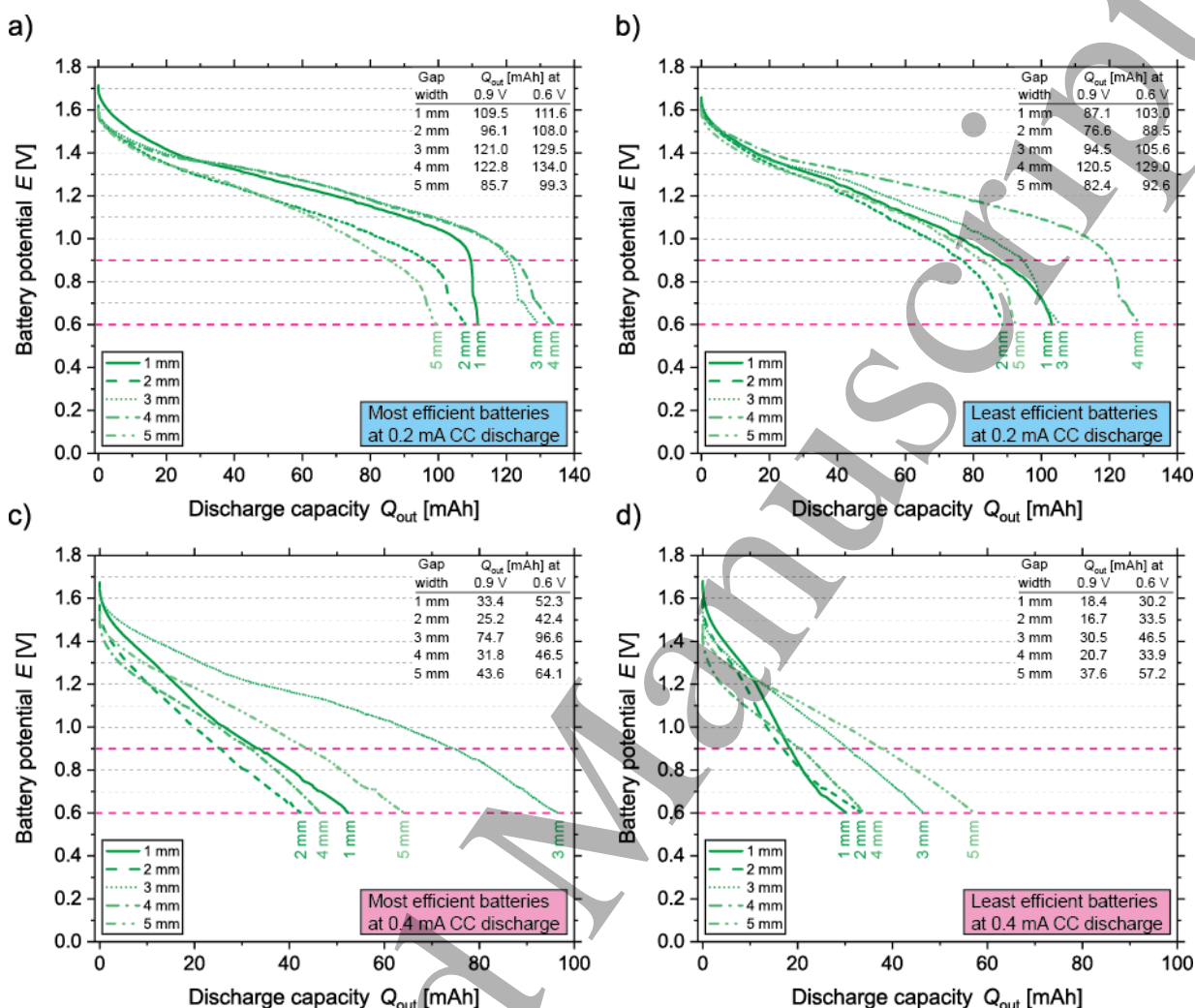


*Figure 6 Discharge curves of (a) the most efficient and (b) least efficient batteries discharged with a 0.2 mA constant current discharge technique. Discharge curves of (c) the most efficient and (d) least efficient batteries discharged with 0.4 mA constant current.*

In Figure 6c, sloping discharge profiles with considerable voltage drops (*IR* drops), especially from the OCP to CCV are observed. In the field of Zn|MnO$_2$ batteries, distinctive *IR* drops are typical for an accelerated depletion of MnO$_2$ and can be related to the increased discharge current [39]. Nonetheless, reduced discharge efficiencies of 15.0 % (1 mm), 12.1 % (2 mm), 12.6 % (4 mm) and 18.8 % (5 mm) are achieved. The battery version with a 3 mm gap exhibits an elevated current rate capability during discharge experiments. Still, the increased discharge current significantly affects the discharge efficiency of this battery which declines to 21.0 %.

Figure 6d reveals exceptional *IR* drops from the OCP to the CCV for all battery configurations. In consequence, discharge capacities of less than 35 mAh are registered for battery versions with gap widths of 1, 2 and 4 mm at the EOD. Slightly increased discharge capacities with 46.5 mAh and 57.2 mAh are recorded for the battery configurations with 3 mm respectively 5 mm gap width. Attributable to the increased discharge current of 0.4 mA, a significant amount of battery capacity seems not to be accessible by electrochemical reaction. Furthermore, absence of observed kinks in the discharge profiles in the potential range of 0.8 V-0.7 V (Figure 6a, b) in the plots of Figure 6c and d suggests incomplete electrochemical reaction of electrode active material.

### 3.2.2 Discharge capacities

Figure 7a provides average discharge capacities $Q_{out}$ of batteries discharged with 0.2 mA CC to 0.9 V and beyond this potential to the EOD of 0.6 V. With 95.8 mAh respectively 95.7 mAh, practically identical values of total discharge capacities were obtained for batteries with gap widths of 2 mm and 5 mm. Maximum values of $Q_{out}$ of 115.7 mAh and 130.8 mAh were achieved for battery configurations with 3 mm and 4 mm gap width. Only small proportions of 7.9 % (3 mm) and 7.2 % (4 mm) on the corresponding total discharge capacity were obtained beyond the battery potential of 0.9 V. Battery versions with 1 mm gap width averaged $Q_{out}$ of 108.1 mAh and represent the median of batteries analysed in this series. Averaging of the results of all batteries discharged with 0.2 mA CC reveals a total $Q_{out}$ of 109.2 mAh with the main part of 98.6 mAh being extracted before and only 10.6 mAh extracted after the 0.9 V potential limit.

The bar chart in Figure 7b illustrates significant differences in average discharge capacities caused by the increased discharge current of 0.4 mA. Compared with the results shown in Figure 7a, all battery configurations show considerable decline in $Q_{out}$ values. Total discharge capacities on same scale were determined for battery configurations with gap widths of 1 mm (42.3 mAh), 2 mm (37.4 mAh) and 4 mm (40.9 mAh). Curve progressions of battery versions with 3 mm and 5 mm gap widths presented in Figure 6c and d demonstrate extended discharge periods under the increased load of 0.4 mA. These results are reflected by increased average discharge capacities of 72.0 mAh (3 mm) and 60.4 mAh for the 4 mm battery configuration. However, the high standard deviation indicated by the whisker should be considered for the classification of the result of the 3 mm battery version when compared with other battery configurations. Overall, a reduced current load capability of the coplanar battery layout is confirmed by the results of the mean discharge capacity of batteries examined in this series. The average total discharge capacity $Q_{out}$ is decreased to 50.6 mAh with 33.4 mAh being discharged until 0.9 V and 17.2 mAh beyond this potential.
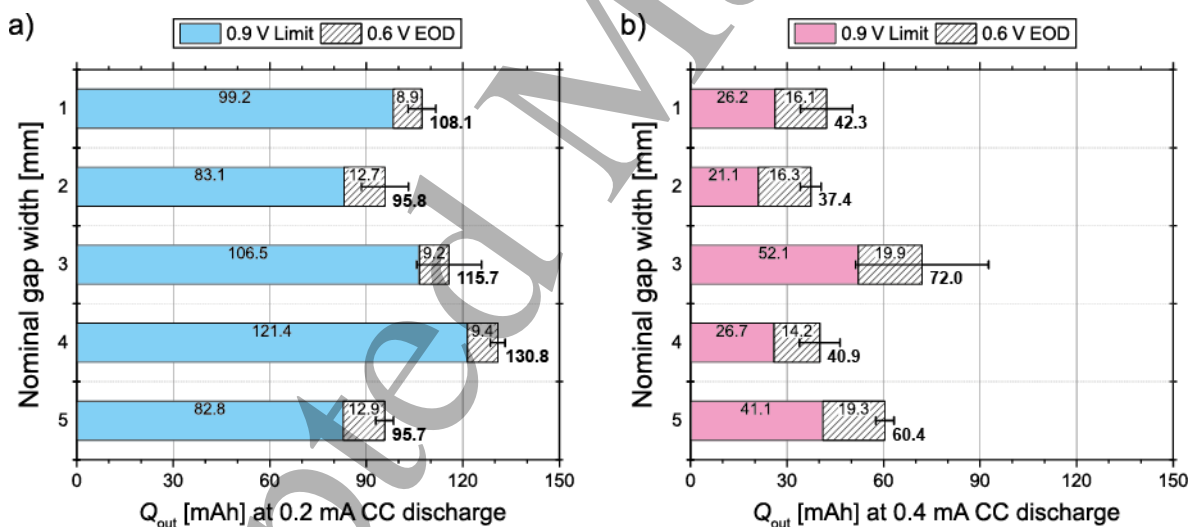


*Figure 7 Averaged discharge capacities of batteries discharged with (a) 0.2 mA and (b) 0.4 mA CC until the 0.9 V limit and to 0.6 V end of discharge (EOD). Total discharge capacities $Q_{out}$ are highlighted in bold. Whiskers indicate the standard deviations of the corresponding measurement series.*

### 3.2.3 Areal capacities

In Figure 8a, areal capacities are presented to improve comparability of determined discharge performances introduced in Figure 7a and b with other printed battery technologies and battery construction principles (i.e. stack-type configuration). As illustrated in Figure 8b, areal capacities are calculated including the interspaces separating both electrodes. Data points coloured in light cyan or light magenta represent areal capacities achieved at the 0.9 V limit.

10

Batteries with gap widths of 5 mm exhibit the lowest areal capacity with 2.0 mAh cm$^{-2}$ at the EOD when being discharged with 0.2 mA CC (Figure 8a). Presumably, the large distance between the electrodes and electrode ageing effects particularly driven by continuous ZnO formation on the anode side promote earlier decline of the electrochemical reaction. Discharged with 0.2 mA CC, batteries consisting of 3 mm and 4 mm interspaces show the highest areal capacities at the EOD with 2.5 mAh cm$^{-2}$ and 2.8 mAh cm$^{-2}$. As discussed in section 3.2.2, discharge capacities are generally affected by the increase of the discharge current which is in accordance with the areal capacities. Except for the 3 mm battery version which shows extended standard deviation values, gap width related differences in calculated areal capacities are hardly visible.
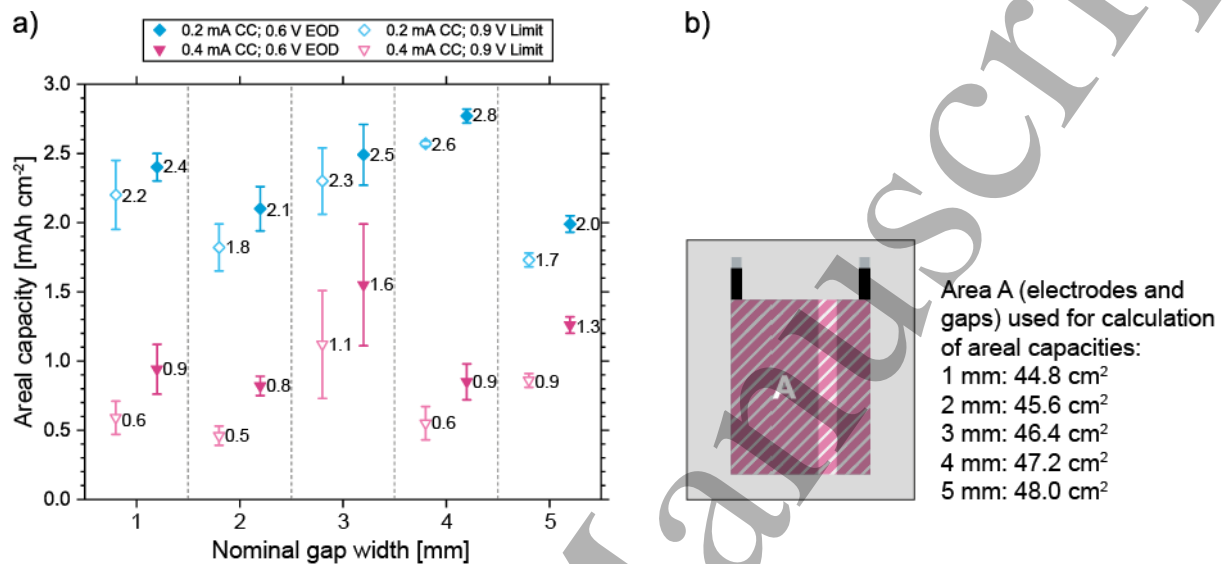


*Figure 8 (a) Areal capacities at different states of charge (SOC) calculated on the basis of averaged discharge capacities including the electrode separating gaps; (b) illustration of areal calculation and corresponding areas for the different battery configurations.*

### 3.2.4 Short circuit currents and internal resistances

The development of internal resistance $R_{in}$ values was monitored by four-terminal sensing 1 kHz AC measurements during battery activation, encapsulation and in 60 min intervals during a subsequently connected 120 min resting phase. As can be seen by the results in Figure 9a, the magnitude of the measured $R_{in}$ values is slightly (1-4 mm) and substantially (5 mm) affected by the nominal gap width of the batteries already before drying. $R_{in}$ values of all battery configurations increase by thermal intake during the drying procedure (75 s, 50 °C) before encapsulation. $R_{in}$ values of battery configurations with small gap widths of 1 mm and 2 mm appear to recover during the resting phase. While the $R_{in}$ of the battery with 1 mm gap width recovers to a nearly identical value of 52.6 Ω just before drying of the electrolyte layer, a slightly elevated value of 77.0 Ω at the end of the 120 min resting phase is observed for the 2 mm battery version. Battery configurations with gap widths of 3 mm and 4 mm show increased but constant $R_{in}$ values during the encapsulation procedure and at the end of the resting phase. However, arranged between 106.3 Ω (3 mm) and 109.4 Ω (4 mm), values have doubled compared to those of the 1 mm battery version. The most significant increase of the 1 kHz internal resistance is observed for the battery configuration with the largest gap width of 5 mm. Besides the increased standard deviation of the $R_{in}$ values, a steady increase over time during the encapsulation process and during the resting phase is recognised. An increase in internal resistance to 153.1 Ω is determined at the end of the 120 min resting period which corresponds triple the value of the 1 mm battery version.

The proximate decrease of $R_{in}$ values observed for batteries with smaller gap widths (1-2 mm) can be interpreted as a cell formation process with a time-dependent progressive penetration of electrolyte into the structure of the electrode [36]. The actual gap width and processes within the electrolyte layers seem to have only marginal effects on $R_{in}$ values. Current collector fabrication was identical for all battery

11

versions (Figure 2c). Transferred masses as well as layer thicknesses of electrodes (Figure 5a, b) allow direct comparison of battery performance metrics within the measurement series. Therefore, $R_{in}$ values seem to be increasingly affected by the respective gap width and the condition of the electrolyte layers in between the gaps. Ionic conductive paths can additionally be impeded by possible air inclusions within the electrolyte layers whose relative occurrence is raised by increasing gap widths. In consequence, the reduction of $R_{in}$ values during cell formation is superseded by the appearance of gap width related resistances.

Additionally, maximum DC short circuit currents were determined for all battery configurations 12 h after battery encapsulation by lamination was performed (Figure 9b). As can be seen, maximum DC short circuit currents decrease linearly with increasing gap widths. While 11.5 mA are achieved for batteries having a gap width of 1 mm, this value is linearly reduced to a third with 3.7 mA for batteries with 5 mm interspace.
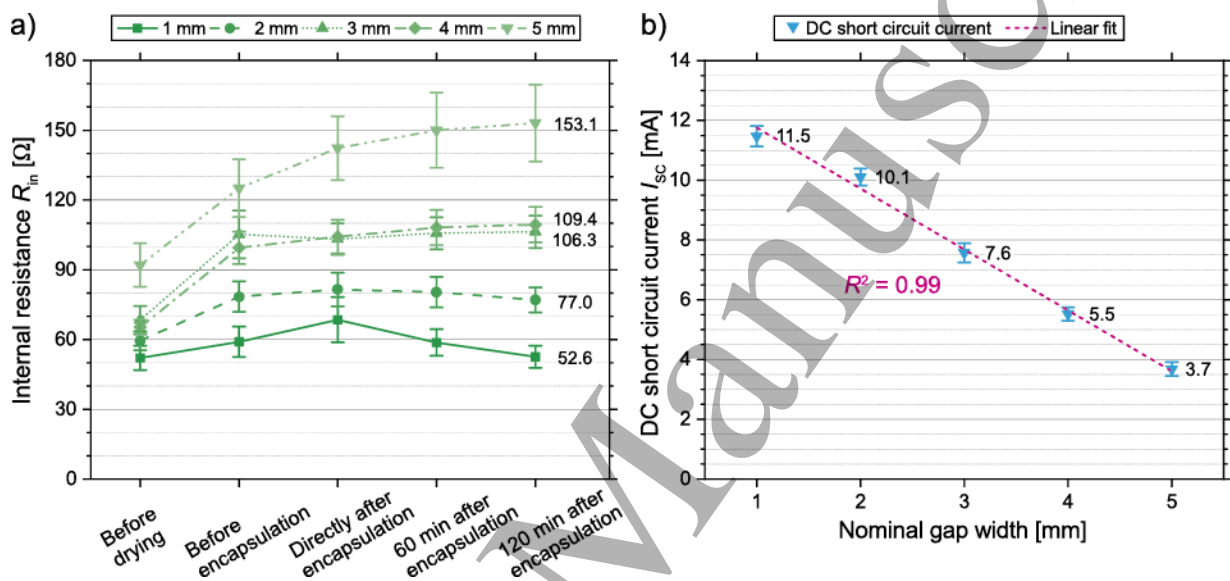


*Figure 9 (a) Averaged internal resistance $R_{in}$ values determined by four-terminal 1 kHz AC sensing measurements at different process stages before and after encapsulation; (b) maximum DC short circuit currents of printed coplanar $Zn/MnO_2$ batteries with varying gap widths.*

### 3.3 Electrochemical impedance measurements

GEIS measurements were performed on batteries discharged with 0.2 mA CC (Figure 6a) to observe and interpret possible changes in electrochemical characteristics at different SOC (Figure 4). The results of the measurements are presented in Nyquist plots in Figure 10a-e at the respective SOC.

In Figure 10a, ascending bulk electrolyte resistance $R_B$ values related to increasing gap widths of the batteries are in correspondence with theory. Before discharge, $R_B$ values with intercepts on the real axis ranging from 31.2 Ω (1 mm gap) to 111 Ω (5 mm) were determined in the 100 kHz frequency range (Table 2). $R_B$ values of batteries with gap widths of 2-4 mm are located close to each other in the range of 53.5 Ω – 69.3 Ω. Interestingly, a significant step in $R_B$ is registered for the 5 mm battery version (111 Ω).

*Table 2 Bulk electrolyte resistances $R_B$ determined at a frequency of 100 kHz at different states of charge (SOC).*

| | | Nominal gap width [mm] | | | | |
|---|---|---|---|---|---|---|
| | State of charge | 1 | 2 | 3 | 4 | 5 |
| | Before discharge | 31.2 | 53.5 | 63.9 | 69.3 | 111 |
| Bulk electrolyte resistance $R_B$ at 100 kHz [Ω] | $Q_{out}$: 2 mAh | 27.6 | 57.9 | 67.0 | 72.1 | 119 |
| | $Q_{out}$: 8 mAh | 30.5 | 68.4 | 73.1 | 78.0 | 144 |
| | $Q_{out}$: 16 mAh | 33.6 | 78.5 | 81.0 | 85.6 | 177 |
| | End of discharge | 60.2 | 110 | 130 | 185 | 269 |

The existence of two consecutive depressed semicircles in the high to mid-frequency range (100 kHz – 4 Hz) can be assumed for all battery versions until a capacity of 16 mAh is drawn (Figure 10a-d). These two semicircles can be represented by two parallel arrangements of a resistor $R$ and a constant phase element *CPE* connected in series. The *CPE* can be regarded as an imperfect capacitator representing the double-layer capacitance and the distributed capacitive behaviour in electrodes consisting of non-homogeneous particles (MnO$_2$ cathode) [41–43]. The diameters of the semicircles can be assigned to the kinetically controlled charge transfer resistance $R_{CT}$ [36, 44]. For the battery version with a 1 mm gap (Figure 10a), an increased sum of $R_{CT}$ of around 150 Ω in the mid-frequency range is observed for both electrodes. The increase in $R_{CT}$ could be explained by incomplete cell formation or inhomogeneities in the printed electrolyte layer filling the small gap.
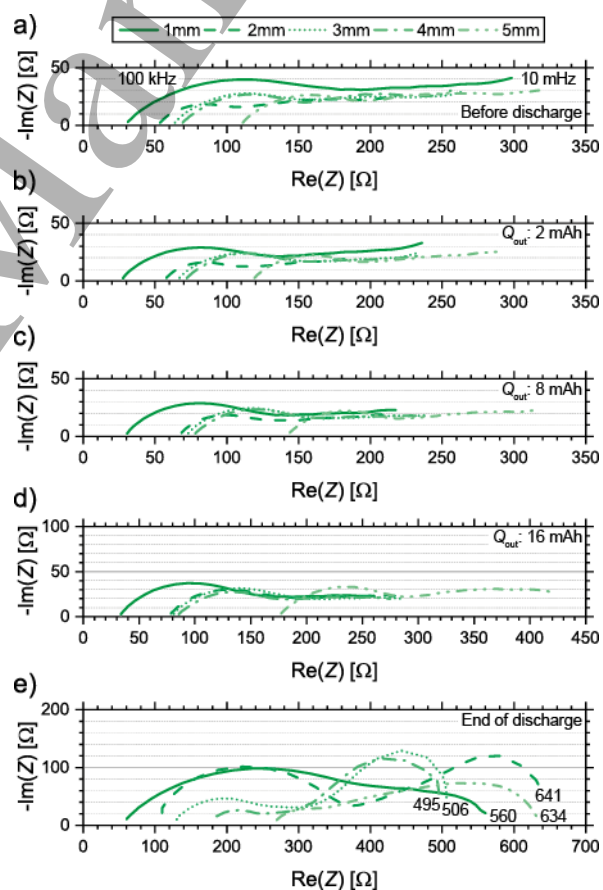


*Figure 10 (a-e) Nyquist impedance plots of batteries with nominal gap widths of 1-5 mm at different states of charge (SOC) recorded in a frequency range between 100 kHz and 10 mHz.*

Characteristic for diffusion related ion transport limitations in the electrolyte and the porous structure of the electrode, lines with moderate gradients lower than 45° are observed in the low-frequency range (10 mHz) for assumable all battery configurations in Figure 10a and b. Continuous flattening of the gradients after extraction of 8 mAh (Figure 10c) to nearly 0° after discharge of 16 mAh (Figure 10d) suggests deploying electrode degradation attributable to a reduced porosity on the cathode side [43]. Early degradation or drying of the electrolyte as the driving factor can be excluded by the results of the corresponding $R_B$ values. As shown in Table 2, $R_B$ values slightly increase over discharge for batteries with gap widths in the range of 1-4 mm while an accelerated increase is recognised for the 5 mm battery version. Typically being characteristic for an advanced ageing of electrodes, substantial increase in low-frequency impedances from around 290 Ω to 420 Ω for the 5 mm battery version is visible in Figure 10b-d [43].

Figure 10e provides information on electrochemical battery characteristics of the five battery versions at the EOD. Increased $R_B$ values determined for all battery versions indicate depletion of electrolyte during discharge collaterally enhanced by the enlargement of gap widths. Distinctive electrode degradation is characterised by increase of $R_{CT}$ values and impedances in the low-frequency range. Both can be attributed to the continuous growth of the actual gap width between the electrodes by formation of insulating ZnO on the anode side (Figure 11a) and a decrease in porosity on the cathode side. The continuous decrease of porosity by discharge of the $MnO_2$ electrode reduces diffusion into the particles of the active mass. At the same time, increase in volume adversely affects conductivity of the $MnO_2$ electrode [43]. The arrangement of impedance values at 10 mHz in Figure 10e follows a negative linear relationship ($R^2 = 0.86$) to the recorded discharge capacities $Q_{out}$ of the respective batteries at the EOD (Figure 6a). Therefore, it can be assumed that individual discharge related electrode degradation processes have stronger impact on the maximum discharge capacity $Q_{out}$ than the $R_B$ value which though is increased by gap width extension.

### 3.4 Post-mortem analysis

Figure 11a provides an overview on batteries with varying gap widths at three different stages of fabrication and battery testing. Image details of the batteries were taken before printing of the electrolyte layer, directly after the EOD and 30 days after reaching the EOD.

Before battery activation, calendered Zn anode surfaces reveal a typical bright metallic appearance without any obvious defects being visible in the electrode layers. Due to the transparent encapsulation film, modification of electrode characteristics and changes inside the gap are clearly visible. The brightness of Zn layers is reduced by printing of electrolyte layers which can be referred to the wetting of electrode structures by the electrolyte. Image excerpts of all batteries at the EOD reveal dark appearing areas growing from the edge of the gap to the right-hand side of the Zn anode. These dark appearing areas indicate the progression of electrochemical conversion of metallic Zn to insulating ZnO during discharge (Equation 1). As a result of this, the actual gap width between both electrodes can be considered to have a dynamic character during discharge. This can be observed by the shifts of the corresponding $R_B$ and $R_{CT}$ values on the real axis in the Nyquist plots in Figure 10a-e. On the cathode side, partial agglomeration of individual greyish particles is visible on the surface of the porous $MnO_2$ based electrode. Beard et al. [39] reference these particles to a complex formation of Zn oxychloride crystals ($Zn_5(OH)_8Cl_2 \cdot H_2O$) which were also evidenced by SEM studies in previous experiments with this battery chemistry [36]. Furthermore, growth of crystalline structures inward the gap is recognisable for battery configurations with gap widths of 1-4 mm. Images recorded 30 days after reaching the EOD evidence progressive growth of these structures for the 3 mm and 4 mm battery configurations. Battery versions with 1 mm and 2 mm gap widths show already established contacts to the $MnO_2$ electrodes.
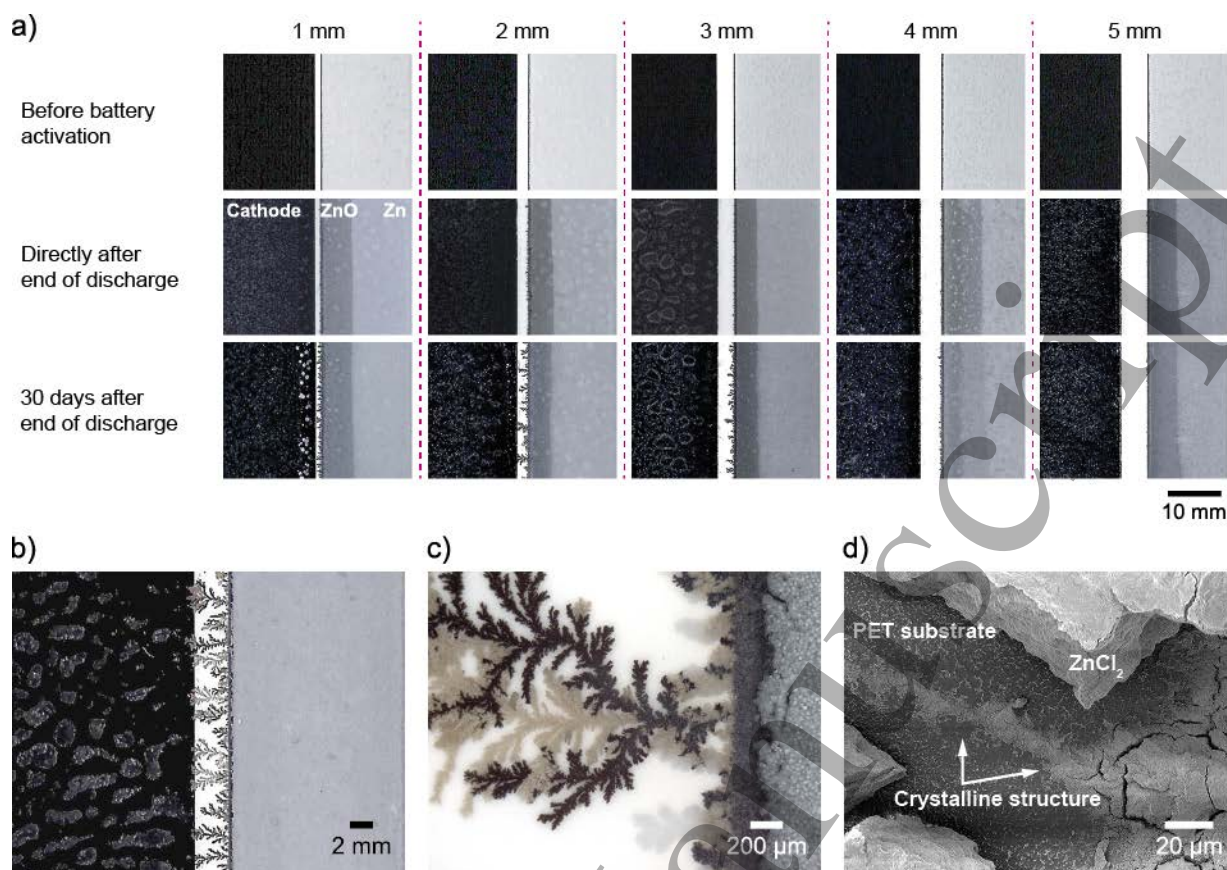
*Figure 11 (a) Excerpts of batteries with varying gap widths before printing of the electrolyte directly after the end of discharge (EOD) and 30 days after reaching the EOD; (b-d) detailed studies of crystalline structures bridging both electrodes after a resting period of more than 90 days using (b, c) white-light microscopy of an encapsulated battery (d) scanning electron microscopy (SEM) after removal of the encapsulation film and drying of the electrolyte.*

Formation of these crystalline structures was also evidenced for batteries only being examined by short circuit capability tests without further discharge (Figure 11b-d). Details of the crystalline structures of a 3 mm battery version recorded after a resting period of more than 90 days are shown in Figure 11b-d. While Figure 11b clearly indicates bridging of the 3 mm gap by the crystalline structures from the Zn anode to the $MnO_2$ cathode, further information on the origin of these structures is provided by Figure 11c. The light grey and black appearing crystalline structures have direct material connection with the carbon black passivation layer, which was confirmed by SEM imaging (Figure 11d). Therefore, disintegration and scouring of printed silver and carbon black layers over time cannot be excluded. It can be assumed that the acidic 5.8 M $ZnCl_2$ electrolyte (pH: 2.3) is responsible for the disintegration of the printed layers. The direction of growth of these crystalline structures from anode to cathode is determined by a previously unnoticed migration effect in the construction principle of printed coplanar $Zn|MnO_2$ batteries.

15

## 4 Conclusion

Fully screen-printed coplanar $Zn|MnO_2$ batteries with equal electrode dimensions and gap lengths were fabricated with varying gap widths in a range of 1-5 mm. GEIS measurements conducted before discharge indicated bulk electrolyte resistances $R_B$ in conformity with increasing gap widths ranging from 31.2 $\Omega$ (1 mm gap) to 111 $\Omega$ (5 mm). DC short circuit currents ranging from 11.5 mA (1 mm) to 3.7 mA (5 mm) revealed a linear decrease by a factor of three instead of five. This observation was verified by 1 kHz AC $R_{in}$ measurements showing increase in battery $R_{in}$ values from 1 mm to 5 mm gap widths by a factor of three. Though discharge curves of batteries drained by a 0.2 mA constant current revealed no gap width related deviations in curve progressions. Maximum discharge capacities $Q_{out}$ not being arranged in a specified order ranged from 99.3 mAh to 134.0 mAh achieving a maximum discharge efficiency ($Q_{out}/Q_{th}$) of 36.4 % with a 4 mm battery version in this study. However, a negative linear relationship of the 10 mHz impedances to the recorded discharge capacities $Q_{out}$ of the respective batteries was determined by GEIS measurements at the EOD.

Further discharge experiments proved that the magnitude of the applied discharge current has a stronger impact on battery discharge capability than the extension of the nominal gap width. In consequence, distinctive $IR$ drops result in sloping discharge curve progressions and reduced discharge capacities of batteries drained by 0.4 mA CC. While there is no specific order of discharge curves that can be assigned to the respective gap width, considerable current related differences in areal capacities were determined at the EOD. The range of areal capacities declined from 2.0-2.8 mAh cm$^{-2}$ (0.2 mA CC) to 0.8-1.6 mAh cm$^{-2}$ (0.4 mA CC). However, the most efficient batteries of this study may compete with reported areal capacities of screen-printed $Zn|MnO_2$ batteries (1.9-3.1 mAh cm$^{-2}$) [30, 31, 35, 45, 46], printed lithium-ion batteries (1.8-2.5 mAh cm$^{-2}$) [11, 47] and printed zinc-air batteries (0.5-2.0 mAh cm$^{-2}$) [48, 49].

Post-mortem analysis of batteries revealed time-dependent formation of crystalline structures growing inward the gap, which may damage the battery by bridging the electrodes. Microscopic studies suggest separation of printed current collectors and passivation layers by the acidic $ZnCl_2$ electrolyte. The specific orientation of the crystalline structures implies the existence of a previously unnoticed migration effect in the coplanar battery architecture.

In summary, the magnitude of the gap width can be regarded as a secondary factor affecting the discharge capability of coplanar $Zn|MnO_2$ batteries if the gap is smaller than 5 mm. Increase of gap widths up to 4 mm enables fabrication of printed batteries even on conventional roll-to-roll printing machinery at high volumes. This could decrease unit costs of this promising battery technology to a significant extent. Further research should be performed to increase the electrode interfacial area by a transformation of the battery design. This could additionally reduce internal resistances and improve battery discharge profiles by elevated voltage plateaus. Comprehensive investigations should be conducted in the field of current collector stability in common electrolyte media for $Zn|MnO_2$ batteries to ensure production of durable printed batteries with stable shelf-live.

**Conflict of interest**

The authors declare they have no potential conflict of interest.

**ORCID iDs**

Timothy C. Claypole      https://orcid.org/0000-0003-1393-9634
Michael Herrenbauer     https://orcid.org/0000-0003-1391-5026
Patrick Rassek         https://orcid.org/0000-0003-0694-7644

1
2
3
4
5
6
7
8
9
10
11
12
13
14
15
16
17
18
19
20
21
22
23
24
25
26
27
28
29
30
31
32
33
34
35
36
37
38
39
40
41
42
43
44
45
46
47
48
49
50
51
52
53
54
55
56
57
58
59
60

## References

[1] Costa C M, Gonçalves R and Lanceros-Méndez S 2020 Recent advances and future challenges in printed batteries *Energy Storage Materials* **28** 216–34

[2] Lanceros-Méndez S and Costa C M (eds) 2018 *Printed Batteries: Materials, technologies and applications* (Chichester, UK: John Wiley & Sons, Ltd)

[3] Sousa R E, Costa C M and Lanceros-Méndez S 2015 Advances and Future Challenges in Printed Batteries *ChemSusChem* **8** 3539–55

[4] Kim B J, Evans J W and Wright P K 2018 Pulsed discharge of printed secondary Zn-MnO2 batteries for IoT and wearable devices *J. Phys.: Conf. Ser.* **1052** 12012

[5] Choi K-H, Ahn D B and Lee S-Y 2018 Current Status and Challenges in Printed Batteries: Toward Form Factor-Free, Monolithic Integrated Power Sources *ACS Energy Lett.* **3** 220–36

[6] Suganuma K 2014 *Introduction to printed electronics (SpringerBriefs in Electrical and Computer Engineering* vol 74*)* (New York, NY, s.l.: Springer New York)

[7] Khan S, Ali S and Bermak A 2019 Recent Developments in Printing Flexible and Wearable Sensing Electronics for Healthcare Applications *Sensors (Basel, Switzerland)* **19**

[8] Sreenilayam S P, Ahad I U, Nicolosi V, Acinas Garzon V and Brabazon D 2020 Advanced materials of printed wearables for physiological parameter monitoring *Materials Today* **32** 147–77

[9] Liu Y, Pharr M and Salvatore G A 2017 Lab-on-Skin: A Review of Flexible and Stretchable Electronics for Wearable Health Monitoring *ACS nano* **11** 9614–35

[10] Khan Y *et al* 2018 A flexible organic reflectance oximeter array *Proceedings of the National Academy of Sciences of the United States of America* **115** E11015-E11024

[11] Ostfeld A E, Gaikwad A M, Khan Y and Arias A C 2016 High-performance flexible energy storage and harvesting system for wearable electronics *Scientific reports* **6** 26122

[12] Bandodkar A J, Jia W and Wang J 2015 Tattoo-Based Wearable Electrochemical Devices: A Review *Electroanalysis* **27** 562–72

[13] K Varadharaj E and Jampana N 2015 Studies on Carbon Mediated Paste Screen Printed Sensors for Blood Glucose Sensing Application *ECS Transactions* **66** 23–33

[14] Payne M E, Zamarayeva A, Pister V I, Yamamoto N A D and Arias A C 2019 Printed, Flexible Lactate Sensors: Design Considerations Before Performing On-Body Measurements *Scientific reports* **9** 13720

[15] Takei K, Honda W, Harada S, Arie T and Akita S 2015 Toward flexible and wearable human-interactive health-monitoring devices *Advanced healthcare materials* **4** 487–500

[16] Xu X, Luo M, He P, Guo X and Yang J 2019 Screen printed graphene electrodes on textile for wearable electrocardiogram monitoring *Appl. Phys. A* **125**

[17] Ray T R, Choi J, Bandodkar A J, Krishnan S, Gutruf P, Tian L, Ghaffari R and Rogers J A 2019 Bio-Integrated Wearable Systems: A Comprehensive Review *Chem. Rev.* **119** 5461–533

[18] Khan Y, Thielens A, Muin S, Ting J, Baumbauer C and Arias A C 2020 A New Frontier of Printed Electronics: Flexible Hybrid Electronics *Advanced materials (Deerfield Beach, Fla.)* **32** e1905279

[19] Pereira A, Bergeret E, Benzaim O, Routin J, Haon O, Tournon L, Coppard R and Depres G 2018 Near-field communication tag development on a paper substrate—application to cold chain monitoring *Flex. Print. Electron.* **3** 14003

[20] Kang H, Park H, Park Y, Jung M, Kim B C, Wallace G and Cho G 2014 Fully roll-to-roll gravure printable wireless (13.56 MHz) sensor-signage tags for smart packaging *Scientific reports* **4** 5387

[21] Lydekaityte J and Tambo T 2019 - 2019 Technological Capabilities of Printed Electronics: Features, Elements and Potentials for Smart Interactive Packaging *2019 Portland International Conference on Management of Engineering and Technology (PICMET) 2019 Portland International Conference on Management of Engineering and Technology (PICMET) (Portland, OR, USA, 8/25/2019 - 8/29/2019)* (IEEE) pp 1–11

17

[22] Grau G, Cen J, Kang H, Kitsomboonloha R, Scheideler W J and Subramanian V 2016 Gravure-printed electronics: recent progress in tooling development, understanding of printing physics, and realization of printed devices *Flex. Print. Electron.* **1** 23002

[23] Wang Z 2013 Flexographically Printed Rechargeable Zinc-based Battery for Grid Energy Storage *Ph.D. Thesis* College of Mechanical Engineering, University of California

[24] Bayer M 2019 Performance of Printed Batteries *Ph.D. Thesis* College of Engineering, Swansea University

[25] Wang X, Zheng S, Zhou F, Qin J, Shi X, Wang S, Sun C, Bao X and Wu Z-S 2020 Scalable fabrication of printed Zn//MnO2 planar micro-batteries with high volumetric energy density and exceptional safety *National Science Review* **7** 64–72

[26] Liu X, Yi J, Wu K, Jiang Y, Liu Y, Zhao B, Li W and Zhang J 2020 Rechargeable Zn-MnO2 batteries: advances, challenges and perspectives *Nanotechnology* **31** 122001

[27] Kim B, Winslow R, Lin I, Gururangan K, Evans J and Wright P 2015 Layer-by-layer fully printed Zn-MnO2 batteries with improved internal resistance and cycle life *J. Phys.: Conf. Ser.* **660** 12009

[28] Saidi A, Desfontaines L, Champeval A, Lebreux J-D, Lecomte C, Pruneau M, Grondein A, Izquierdo R and Bélanger D 2017 The effect of ink formulation and electrode geometry design on the electrochemical performance of a printed alkaline battery *Flex. Print. Electron.* **2** 15002

[29] Lao-atiman W, Julaphatachote T, Boonmongkolras P and Kheawhom S 2017 Printed Transparent Thin Film Zn-MnO2 Battery *J. Electrochem. Soc.* **164** A859-A863

[30] Madej E, Espig M, Baumann R R, Schuhmann W and La Mantia F 2014 Optimization of primary printed batteries based on Zn/MnO2 *Journal of Power Sources* **261** 356–62

[31] Wendler M, Steiner E, Claypole T C and Krebs M 2014 Performance optimization of fully printed primary (ZnMnO2) and secondary (NiMH) batteries *Journal of Print and Media Technology Research* **III** 241–51

[32] Willfahrt A, Fischer T, Sahakalkan S, Martinez R, Krebes M and Steiner E 2018 Parameter evaluation of printed primary Zn/MnO2 batteries with nonwoven and hydrogel separators *Flex. Print. Electron.* **3** 45004

[33] Wendler M, Hübner G and Krebs M 2011 Development of Printed Thin and Flexible Batteries *International Circular of Graphic Education and Research* **4** 32–41

[34] Willert A and Baumann R R 2013 Customized printed batteries driving sensor applications *2013 International Semiconductor Conference Dresden-Grenoble (ISCDG): 26 - 27 Sept. 2013, Dresden, Germany; technology, design, packaging, simulation and test; international conference and table top exhibition 2013 International Semiconductor Conference Dresden - Grenoble (ISCDG) (Dresden, Germany, 9/26/2013 - 9/27/2013)* ed G Schmidt (Piscataway, NJ: IEEE) pp 1–4

[35] Willert A, Meuser C and Baumann R R 2018 Printed batteries and conductive patterns in technical textiles *Jpn. J. Appl. Phys.* **57** 05GB02

[36] Rassek P, Steiner E, Herrenbauer M and Claypole T C 2019 The effect of electrode calendering on the performance of fully printed Zn|MnO2 batteries *Flex. Print. Electron.* **4** 35003

[37] Grillo-Werke Aktiengesellschaft M D 2017 *Zinc Powder Type G007-pe: Certificate of Analysis* (Goslar)

[38] Hioki E.E. Corporation 2018 *User manual: BT3562 Battery HiTester* (accessed 11 Feb 2019)

[39] Beard K W, Reddy T B and Linden D 2019 *Linden's handbook of batteries* (New York: McGraw-Hill)

[40] Zamarayeva A M, Jegraj A, Toor A, Pister V I, Chang C, Chou A, Evans J W and Arias A C 2020 Electrode Composite for Flexible Zinc–Manganese Dioxide Batteries through In Situ Polymerization of Polymer Hydrogel *Energy Technol.* **8** 1901165

[41] Barsoukov E and Macdonald J R (eds) 2018 *Impedance spectroscopy: Theory, experiment, and applications* (Hoboken, NJ: Wiley)

[42] Oladimeji C F, Moss P L and Weatherspoon M H 2016 Analyses of the Calendaring Process for Performance Optimization of Li-Ion Battery Cathode *Advances in Chemistry* **2016** 1–7

[43] Jossen A 2006 Fundamentals of battery dynamics *Journal of Power Sources* **154** 530–8

[44] Bio-Logic Science Instruments 2010 *Zfit and equivalent electrical circuits (EC-Lab Application Notes* 14*)* (Claix)

[45] Choi M G, Kim K M and Lee Y-G 2010 Design of 1.5 V thin and flexible primary batteries for battery-assisted passive (BAP) radio frequency identification (RFID) tag *Current Applied Physics* **10** e92-e96

[46] Lee Y-G, Choi M-G, Kang K-Y and Kim K-M 2010 Preparation and Electrochemical Performance of 1.5 V and 3.0 V-Class Primary Film Batteries for Radio Frequency Identification (RFID) *Journal of Electrochemical Science and Technology* **1** 39–44

[47] Kang K-Y, Lee Y-G, Shin D O, Kim J-C and Kim K M 2014 Performance improvements of pouch-type flexible thin-film lithium-ion batteries by modifying sequential screen-printing process *Electrochimica Acta* **138** 294–301

[48] Hilder M, Winther-Jensen B and Clark N B 2009 Paper-based, printed zinc–air battery *Journal of Power Sources* **194** 1135–41

[49] Ma T and Devin MacKenzie J 2019 Fully printed, high energy density flexible zinc-air batteries based on solid polymer electrolytes and a hierarchical catalyst current collector *Flex. Print. Electron.* **4** 15010